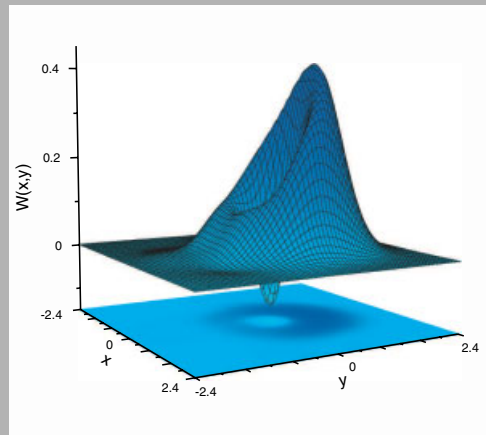


Abstract: We report about the realization and the applications of an efficient pulsed optical homodyne apparatus operating in the time domain at the high repetition rates characteristic of commonly used mode-locked lasers for the analysis of quantum light states. We give a full characterization of our system by shot-noise measurements and by verifying its capability to work in a gated configuration at lower acquisition rates. We demonstrate the potential of this high-frequency time-domain detector by applying it to the reconstruction of the density matrix elements and of the Wigner functions of various field states by means of quantum tomography. Results are shown for the complete characterization of simple coherent states with low average photon number, of single-photon Fock states and of the so-called single-photon added coherent states, which result from the elementary excitation of a classical wave-like field. Wigner functions with negative values are observed for the non-classical states and an overall efficiency of about 60% is obtained for the generation/detection system.



Reconstructed Wigner function of a single-photon-added coherent state (SPACS)

© 2006 by Astro Ltd.
Published exclusively by WILEY-VCH Verlag GmbH & Co. KGaA

Non-classical field characterization by high-frequency, time-domain quantum homodyne tomography

A. Zavatta,^{1,2,*} S. Viciani,^{1,2} and M. Bellini^{1,2,*}

¹ Istituto Nazionale di Ottica Applicata, 6, L. go E. Fermi, I-50125, Florence, Italy

² LENS and Department of Physics, University of Florence, I-50019 Sesto Fiorentino, Florence, Italy

Received: 18 July 2005, Accepted: 25 August 2005

Published online: 26 September 2005

Key words: nonclassical states; optical homodyne tomography

PACS: 42.50.Dv, 03.65.Wj

1. Introduction

Balanced homodyne detection provides a measurement of the field quadratures [1–3] allowing the quantum characterization of a field mode by the reconstruction of its density matrix elements and Wigner function [4]. It consists in mixing the unknown signal field with a strong reference local oscillator (LO) field on a 50% beam splitter whose outputs are then detected by proportional photodetectors. The difference in the photocurrents produced by the two detectors is proportional to the electric field quadrature selected by varying the relative phase between the LO and the signal field [5,6]. From a collection of field quadratures

it is then possible to reconstruct the quantum state by means of quantum tomography techniques [6,7].

The reconstruction of the quantum state of an optical field was first demonstrated in 1993 by Smithey et al. [8,9] when the state of a squeezed vacuum field, generated by an optical parametric amplifier pumped by a pulsed laser was reconstructed by means of its Wigner function. In their experiment the balanced homodyne apparatus worked in the time domain, i.e. the difference between the two photocurrents for each laser pulse was singularly electronically integrated yielding the photon number difference which was used to build-up the field-quadrature distribution. Later, this technique has been extended to describe field states in the cw regime, using a frequency domain approach in

* Corresponding author: e-mail: azavatta@ino.it; bellini@inoa.it

order to analyze quantum states where the difference photocurrent from homodyne detectors is analyzed in a narrow band frequency region away from DC in order to avoid low-frequency technical noise. In particular, using such a kind of apparatus, the group of Mlynek obtained the complete quantum reconstruction of bright and vacuum squeezed states [10, 11], while other kinds of classical and squeezed states have also been investigated by different groups [12, 13]. The frequency-domain approach for homodyne analysis has also been used to characterize pulsed field modes, where signal and local oscillator are provided by pulsed lasers [14, 15]; in this case the homodyne signal results from the average over many pulses and is analyzed in frequency windows far from the laser repetition frequency and its harmonics.

In order to investigate states of light exhibiting stronger non-classical features, pulsed lasers are required for two main reasons: to exploit the stronger nonlinear effects caused by the higher peak intensity and to provide a synchronization clock which gives the opportunity to prepare the state in a conditional way. However, the conditional preparation of non-classical states requires an homodyne apparatus able to detect them, i.e. a time-domain homodyne scheme allowing the detection of certain properly selected pulses only.

Recently, nonclassical states of light with a negative-valued Wigner's quasi-probability distribution have been successfully observed using a conditional preparation scheme and a time-domain homodyne measurement. Firstly, the single-photon Fock state has been generated by a conditional measurement on photon pairs emitted by spontaneous parametric downconversion and fully characterized by the group of Lvovsky [16]. Displaced Fock states, obtained by mixing a coherent state with a single photon upon a highly reflecting beam splitter as in [17], have also been investigated and have shown the non-Gaussian character of their marginal distributions and negative values of the Wigner function. With the same setup, the preparation and characterization of a superposition state of vacuum and single photon has been achieved by the conditional measurement on the previously unused beamsplitter output [18]. In addition, the experimental implementation of quantum scissors [19] in the context of quantum teleportation, the remote preparation of a photonic qubit [20] and the characterization of a single photon delocalized over two spatial modes [21], have been realized and studied by means of time-domain homodyne detection. Moreover, other non-classical states have been recently produced starting from a squeezed vacuum and with the controlled subtraction of a single photon: in this case the marginal distributions clearly showed a squeezed and non-Gaussian character but the preparation and detection efficiency was not high enough to reconstruct a negative-valued Wigner function [22].

In general, all the time-domain, pulsed, balanced homodyne detectors used for quantum homodyne tomography so far [8, 23–25] have been operated at relatively low frequencies compared to the repetition rate of the com-

monly used pump mode-locked lasers. Due to the dead time of the low-noise charge amplifiers used in those applications, the maximum pulse acquisition rates achievable have been limited to well below the megahertz. Consequently, pulse-pickers [16, 17] or low-repetition-rate lasers have been used to match the frequency response of the detection apparatus, with the drawback of long measurement times that might introduce unwanted fluctuations arising from the phase instabilities of the optical setup. In order to access quantum states with a low generation probability, a time-domain homodyne detection capable to work at the high repetition rate of mode-locked lasers is required. The task of performing time-domain homodyne detection at such high repetition rates is however quite demanding, since it requires very low electronic noise and high subtraction efficiencies over very large frequency bandwidths.

In this review we present an homodyne apparatus which is able to perform high-frequency (with repetition rates up to about 100 MHz) time-domain analysis of quantum states of light [26]. We give a full characterization of our system by measuring the laser shot noise, and demonstrate the ability of the time-domain analysis to reveal the quantum features of the field by comparing its results with those coming from a more conventional spectral approach. We also discuss the capability of our system to work in a gated configuration at lower acquisition rates. By allowing us to perform ultrafast pulse-selective measurements, this apparatus exhibits two main advantages over alternative schemes working at lower repetition rates: on one side, thanks to the much shorter acquisition times, the stability requirements of the overall experimental system are loosened; on the other, if long-term stability of the setup is available, states exhibiting stronger non-classical features (usually characterized by smaller generation probabilities) can be efficiently analyzed.

Here, we also review some of the recent results obtained with this homodyne apparatus able to reach an overall quantum efficiency of about 60%: in particular we describe the complete tomographic reconstruction of a single-photon Fock state [27] with the detailed illustration of the experimental apparatus and the experimental generation of single-photon added coherent states (SPACs) and their complete tomographic characterization [28].

2. Quantum homodyne tomography and state reconstruction

To reconstruct the quantum state of the radiation field we need a series of observables, called field quadratures, that can be provided by means of balanced homodyne detection technique [1–3, 29, 30]. Such technique consists in the detection of the interference products at the outputs of a 50% beam splitter (BS) where the signal field interferes with a strong coherent field called local oscillator (LO). The two output channels of the beam splitter are detected by proportional photodetectors and the two photocurrents are subtracted.

If we call \hat{a} the annihilation operator that describes the signal field and \hat{a}_{LO} the same operator for the local oscillator, we can write the two fields at the output of the BS as

$$\hat{a}_1 = \frac{1}{\sqrt{2}}(\hat{a} + \hat{a}_{LO}) \quad \text{and} \quad \hat{a}_2 = \frac{1}{\sqrt{2}}(\hat{a} - \hat{a}_{LO}), \quad (1)$$

thus the photon number difference operator between the two BS channels is written as

$$\hat{n}_{12} = \hat{n}_1 - \hat{n}_2 = \hat{a}^\dagger \hat{a}_{LO} + \hat{a}_{LO}^\dagger \hat{a}. \quad (2)$$

When the local oscillator is a strong coherent field such that it can be assumed classical, the photon number difference operator becomes

$$\hat{n}_{12} = |\alpha| (\hat{a}^\dagger e^{i\theta} + \hat{a} e^{-i\theta}). \quad (3)$$

Defining the two orthogonal field quadratures as $\hat{x} = (\hat{a} + \hat{a}^\dagger)/2$ and $\hat{y} = i(\hat{a}^\dagger - \hat{a})/2$ (with $[\hat{x}, \hat{y}] = i/2$), we obtain that the integrated photocurrent difference is thus proportional to the signal electric field quadrature $\hat{x}_\theta = \hat{x} \cos \theta + \hat{y} \sin \theta$, where θ is the relative phase imposed between the LO and the signal. Therefore, by performing a series of homodyne measurements on equally-prepared states, the probability distributions $p(x, \theta)$ of the quadrature operator $\hat{x}_\theta = (\hat{a}^\dagger e^{i\theta} + \hat{a} e^{-i\theta})/2$ can be readily obtained.

According to Vogel and Risken [4], the probability distribution $p(x, \theta)$ is equal to the marginal distribution of the Wigner function $W(x, y)$:

$$p(x, \theta) = \int dy W(x \cos \theta - y \sin \theta, x \sin \theta + y \cos \theta). \quad (4)$$

It follows that if we collect probability distributions for different $\theta \in [0, \pi)$ we obtain the homodyne ensemble that is, by definition, the Radon transform of the Wigner's quasi-probability distribution. In principle, given a sufficient number of quadrature distributions for different values of θ , one is able to reconstruct the Wigner function by inverting Eq. (4).

The inverse Radon transform (IRT) is usually written as the phase integral over the marginals convolved with the kernel function $K(z)$:

$$W(x, y) = \int_0^\pi \frac{d\theta}{2\pi^2} \int_{-\infty}^{+\infty} dx' p(x', \theta) K(x_\theta - x'), \quad (5)$$

where $x_\theta = x \cos \theta + y \sin \theta$, the kernel $K(z)$ is given by

$$K(z) = \frac{1}{2} \int_{-\infty}^{+\infty} d\xi |\xi| e^{i\xi z}. \quad (6)$$

This kernel exists only in the sense of a generalized function and, in order to numerically implement the IRT, it is necessary to introduce a cut-off k_c in the integration domain of the integral in Eq. (6). Thus, the kernel can be approximated by

$$K(z) = \frac{1}{z^2} [\cos(k_c z) + k_c z \sin(k_c z) - 1] \quad (7)$$

for $|k_c z| > 0.1$ and by a fourth-order expansion around the origin [6]. The cut-off parameter k_c has to be adjusted according to the state in order to avoid low resolution (since the regularized kernel acts like a smoothing filter) or the introduction of artifacts that render the reconstructed state more classical.

Some simplification in the reconstruction procedures can be accomplished when the Wigner function is phase-invariant [16] like for Fock states. Assuming the cylindrical symmetry of the analyzed state, only one phase-averaged marginal distribution is required for the reconstruction. The Abel transform then can be used instead of IRT in order to reconstruct a section of the Wigner function $W(r)$ [6], as given by

$$W(r) = -\frac{1}{\pi} \int_r^{+\infty} \frac{dx}{\sqrt{x^2 - r^2}} \frac{\partial p_{av}(x)}{\partial x}, \quad (8)$$

where $p_{av}(x)$ is the phase-averaged marginal distribution and $r = \sqrt{x^2 + y^2}$. Due to the singularity for $x = r$, the numerical implementation of this method is however extremely sensitive to noise and a large number of data is required to obtain a reliable result. This reconstruction procedure involves the application of numerically-unreliable methods, and assumptions on the reconstructed state.

Due to the limitations of the "classical-like" tomographic methods described above, the group of D'Ariano has developed a quantum homodyne tomography method based on the statistical averaging of the so called pattern functions, that permits the reconstruction of the density matrix elements directly from the homodyne data [31] without any assumption nor arbitrary parameter.

The elements of the density matrix $\hat{\rho}$ of the state in the number-state representation can be obtained by averaging the pattern functions $f_{nm}(x, \theta)$ over the outcomes of the quadrature operator and over the phase θ as

$$\text{Tr}[\hat{\rho}|m\rangle\langle n|] = \int_0^\pi \frac{d\theta}{\pi} \int_{-\infty}^{+\infty} dx p(x, \theta) f_{nm}(x, \theta), \quad (9)$$

where the pattern functions can be implemented for unit quantum efficiency with stable numerical algorithms [6, 7]. The phase term in the pattern functions appears as $f_{nm}(x, \theta) = F_{nm}(x) e^{i(m-n)\theta}$ which is null for the diagonal elements thus the photon number distribution can be recovered from homodyne data without any phase information as

$$\rho_{n,n} = \int_{-\infty}^{+\infty} dx p_{av}(x) F_{nn}(x), \quad (10)$$

where p_{av} is the phase-averaged marginal distribution.

The above transformations allow to obtain the density matrix elements directly from the homodyne data with-

out building quadrature histograms calculating directly the function averages as

$$\rho_{n,m} = \frac{1}{N} \sum_{i=1}^N f_{nm}(x_i, \theta_i). \quad (11)$$

In addition, it is important to note that the quantum homodyne tomography method gives the opportunity to estimate the reconstruction confidence interval by the well known formula

$$\delta\rho_{n,m} = \sqrt{\frac{\sum_{i=1}^N [f_{nm}(x_i, \theta_i) - \rho_{n,m}]^2}{N(N-1)}} \quad (12)$$

for the standard error of the mean.

Once the density matrix elements are reconstructed, the Wigner function can then be obtained by means of the following transformation:

$$W(x, y) = \sum_{n,m} \rho_{n,m} W_{n,m}(x, y), \quad (13)$$

where $W_{n,m}(x, y)$ is the Wigner function of the operator $|n\rangle\langle m|$. Note that, using this procedure, the Wigner function of the state is reconstructed from a truncated density matrix of dimension $M \times M$. This implies a finite resolution in the reconstructed function which, however, can be adapted to the particular physical situation of interest in order to avoid loss of information on the state. As reported in [7, 32], the above transformation read as:

$$W(x, y) = \text{Re} \sum_{d=0}^M e^{id \arctan(\frac{y}{x})} \sum_{n=0}^{M-d} A_{nd}(x, y) \rho_{n,n+d} \quad (14)$$

and

$$A_{nd}(x, y) = \frac{2(-1)^n}{\pi} [2 - \delta_{d0}] |2(x + iy)|^d \times \times \sqrt{\frac{n!}{(n+d)!}} e^{-2(x^2+y^2)} L_n^d [4(x^2 + y^2)], \quad (15)$$

where $L_n^d(x)$ are Laguerre polynomials, δ is the Kronecker delta and M is the maximal quantum number of the reconstructed density matrix.

Recently, alternative reconstruction techniques based on maximum-likelihood estimation methods have been proposed [33, 34] and used to analyze experimental data [20]. Such methods can reconstruct the density matrix elements and the Wigner function with lower requirements on the number of data samples without a substantial increase in the statistical errors. The implementation of these methods might contribute to further decrease the acquisition time of our experiment whenever this becomes a limiting factor, i.e. when more exotic quantum states are analyzed. Some of these methods [33] require minimization algorithms with M^2 free parameters thus their application is suitable for those cases where the truncated Hilbert space dimension M can be set to few photons.

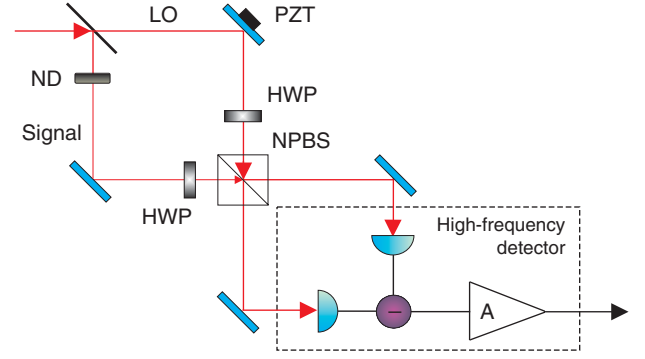


Figure 1 (online color at www.lphys.org) Experimental setup: LO local oscillator beam; HWP half-wave plate; NPBS non-polarizing beam-splitter; A amplifier; PZT piezo-electric transduction stage; ND neutral density filter

3. Noise analysis of an homodyne detector

3.1. Experimental apparatus

For the noise analysis of our homodyne detector, the experimental setup shown in Fig. 1 has been used. Here a mode-locked Ti:sapphire laser (Spectra-Physics Tsunami), emitting 3-ps pulses at a central wavelength of 786 nm, and at a repetition rate of 82 MHz, is used as the source for the local oscillator (LO) beam. The total laser power can be varied by means of a half-wave plate followed by a polarizer. A 50% cube beam-splitter mixes the LO with the field state under study and two 80-mm lenses focus the output beams onto the photodetectors. Since the beam-splitter is not perfectly insensitive to polarization, the balance between its two output ports is finely adjusted using half-wave plates. For the characterization of the detector noise, the signal port of the beam-splitter is blocked, so that only the vacuum field enters the apparatus.

In the first version of the homodyne detector, two pin photodiodes (PD) (EG&G FFD040, with active area diameter of 1 mm) are connected together and oppositely biased. The signal generated is amplified with gain about 10 by an operational amplifier (Comlinear CLC 425) in a non-inverting configuration. The output signal is then recorded by a spectrum analyzer or by a digital scope. The scope (LeCroy LC564) is provided with an analog bandwidth of 1 GHz, a sampling rate of 4 GSamples/s, a vertical resolution of 8 bits and a storage depth of 200,000 points. The detection efficiency for each photodiode, including the spatial collection efficiency, is measured by comparing the reading of a power meter with the mean photocurrent. We obtain $\eta_1 = 0.85 \pm 0.03$ and $\eta_2 = 0.83 \pm 0.03$ for $D1$ and $D2$, respectively.

3.2. Frequency analysis

The frequency response of a single amplified PD is measured by illuminating it with the thermal light from a halo-

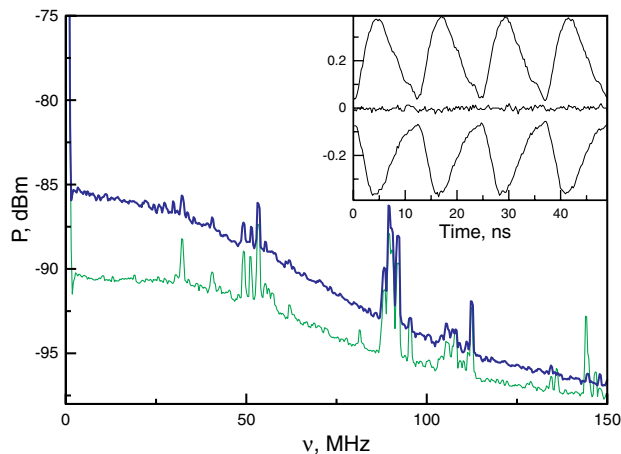


Figure 2 (online color at www.lphys.org) Thick line: spectral power of the detected signal when one photodiode is illuminated by thermal light, giving a photocurrent of 1.16 mA. The resolution bandwidth is 300 kHz. Thin line: electronic noise. The narrow peaks are due to pick-up from environmental noise. Inset: time-domain output signal with the laser impinging only one photodiode (the upper and the lower traces correspond to the signals from the two detectors) and on both photodiodes (middle trace)

gen lamp. A typical measured spectrum is shown in Fig. 2 for a photocurrent of 1.16 mA.

By directing the laser pulse train on the PDs, we have checked that their frequency response curve is broad enough to isolate single pulses in the detected signal. The output pulses show a FWHM duration of about 5 ns and successive pulses, separated by 12 ns, result well distinct from each other as shown in the inset of Fig. 2. This is the first important feature when we want to perform measurements only on particular events, selected by an external gate. The high temporal resolution minimizes the overlap of adjacent pulses. A fit of the output pulses with a double exponential function shows that 93% of the pulse energy is contained within the 12 ns window.

Another key point of the apparatus is its ability to efficiently perform the difference between the amplitude fluctuations of the beams impinging on the two detectors. This is expressed by the Common Mode Rejection Ratio (CMRR) of the balanced detection, defined as the spectral power measured when both PDs are illuminated, divided by the power measured on one PD when the other one is blocked. We have measured it at the harmonic frequencies of the laser repetition rate, obtaining a CMRR of 42 dB, 15 dB, and 20 dB, respectively for the first, second, and third harmonic of the laser repetition rate. The higher harmonics exhibit lower CMRR due to the different response of the two PDs at higher frequencies. The best CMRR is obtained by optimizing both the half-wave plate of the balanced detection and the bias of each PD. The measurements are performed at low laser power in order to avoid

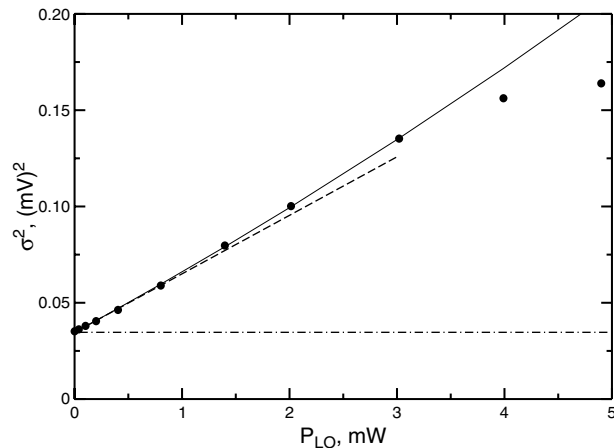


Figure 3 Dots: integral of the power spectrum. Solid line: quadratic fit. Dashed line: shot-noise contribution. Dash-dotted line: electronic noise

saturation of the amplifier by the unbalanced photocurrent when one PD is blocked.

We have performed a test on the effective capability of the detection system to measure the quantum fluctuations of the signal by checking that, when the input signal is the vacuum state, one can really measure the shot-noise of the local oscillator. This is done by acquiring the noise spectrum for different values of the laser power impinging on the PDs. The frequency integral of the power spectrum is plotted as a function of the detected laser power in Fig. 3, together with a second order polynomial fit. We have carried out the integration between 300 kHz and 150 MHz, excluding the peak at the laser repetition rate. The constant term in the fitting function gives the electronic and thermal noise; the first-order term corresponds to the laser shot noise (indicated in Fig. 3 by a dashed line); the second-order term is due to the residual laser excess noise after the balanced detection. The relevant signal in a homodyne detection is carried by the first-order term, while both the constant and the second-order terms give rise to unwanted excess Gaussian fluctuations. The optimum working power is around 3 mW, where about 70% of the fluctuations can be attributed to the first-order term. Above this power, saturation effects appear. Saturation is frequency-dependent: in the dc signal it does not appear up to about 15 mW, while it becomes more important for higher frequencies. In order to avoid signal distortion and questionable measurements, we have limited the laser power to 3 mW for measurements with this apparatus.

3.3. Time-resolved analysis

The previous spectral analysis applies particularly well to a “quasi-cw” measurement system. Indeed the spectral properties are measured by the spectrum analyzer by means of

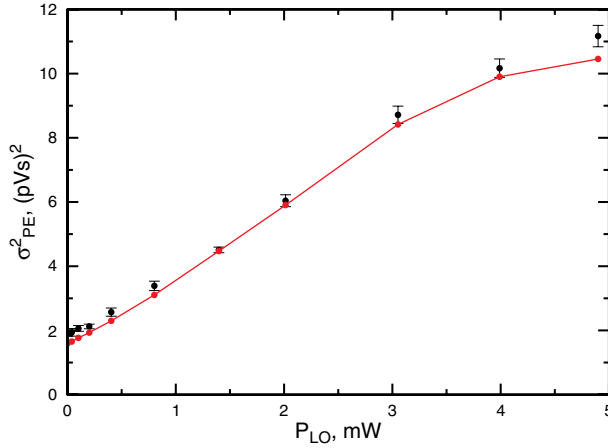


Figure 4 (online color at www.lphys.org) Black filled circles with error bars: σ_{PE}^2 directly measured in the time domain; red filled circles: variance deduced from the spectrum according to Eq. (16)

a time integration over the sequence of laser pulses. Instead, our apparatus has the important additional property that the detection bandwidth allows pulse-selective experiments. It is therefore possible to evaluate properties of the pulsed light by considering the different pulses as separate events and to perform measurements in the time-resolved regime. In this case the output difference signal from the amplifier is stored in the digital scope. Time sequences of 200,000 samples, covering time windows of 50 μ s and including 4000 pulses each, are numerically integrated over time intervals of length $T = 12$ ns, corresponding to the separation between successive pulses, in order to extract the areas of all the pulses in the sequence and perform statistics.

In particular, we have evaluated the variance σ_{PE}^2 of the pulse energy over the recorded time series for different values of the laser average power, as shown in Fig. 4. This time-resolved analysis is directly related to the spectral analysis by

$$\sigma_{PE}^2 = 2 \int_0^{\infty} S(\nu) |f(\nu)|^2 d\nu, \quad (16)$$

where $|f(\nu)|$ is the weight function due to the time integration over the rectangular window corresponding to the pulse duration T , that is found by the Fourier transform

$$f(\nu) = \int_{-T/2}^{T/2} e^{-2\pi i \nu t} dt = T \frac{\sin(\pi \nu T)}{\pi \nu T}. \quad (17)$$

The variance σ_{PE}^2 evaluated from the measured noise spectra according to Eq. (16) is also reported in Fig. 4. It shows a very good agreement with the direct time-domain

measurements, thus confirming the correctness of our approach.

A more refined time-resolved analysis on the pulse sequences stored in the scope has been also performed based on the so-called Allan variance [35]. This is a widely used indicator in metrology and allows to quantify the stability of a parameter on different time scales. The analysis has allowed us to identify the main sources of noise in this setup as those coming from the low-frequency fluctuations in the digital scope electronics [26]. It is also interesting to note that an appropriate choice of the time scale for the measurement of the Allan variance can open the possibility to observe and analyze quantum effects which are overwhelmed by classical fluctuations for different time scales, in a way similar to what happens in the frequency analysis when one chooses a particular spectral region.

4. Homodyne tomography of weak coherent states

To perform a first test of actual homodyne tomography with our high-frequency acquisition technique, we have used the apparatus shown in Fig. 1. A fraction of the laser power is split off the main (LO) beam and enters the second port of the beam-splitter as a test coherent state $|\alpha\rangle$. We first achieve a good spatio-temporal overlap between this signal field and the LO by carefully adjusting the alignment mirrors and the path lengths (by means of two optical delay lines not shown in the figure) in the two arms of the so-formed Mach-Zender interferometer to obtain high-visibility interference fringes. Then the signal beam is strongly attenuated by means of calibrated neutral density filters and the beam path length in the LO arm is correspondingly compensated. The relative phase between the two fields is controlled by applying a voltage to a piezoelectric transducer holding one of the mirrors in the LO beam path.

We have performed measurements of coherent states with different average photon numbers, ranging from 0 to about 5. Each measurement consists of 8 sequences of 4,000 pulses for each of 25 values of the relative phase in the $[0, \pi]$ interval, for a total of 800,000 points per coherent state. In Fig. 5 the areas of some of the acquired pulses are shown. The signal represents the quadratures of the electric field as the phase is varied by means of the PZT stage. In this case the coherent state has a mean number of photons $\langle n \rangle = 0.16$ photons/pulse. Note that this is a sort of "effective" mean photon number which includes all the losses and inefficiencies of the detection system. The "actual" coherent state amplitude impinging on the balanced homodyne beam splitter is actually larger (i.e. $|\alpha| > \sqrt{\langle n \rangle}$).

For each value of the relative phase θ between the LO and signal fields the histogram of the measured pulse energy difference represents the distribution $p(x, \theta)$ of the specific phase-rotated quadrature. The collection of the

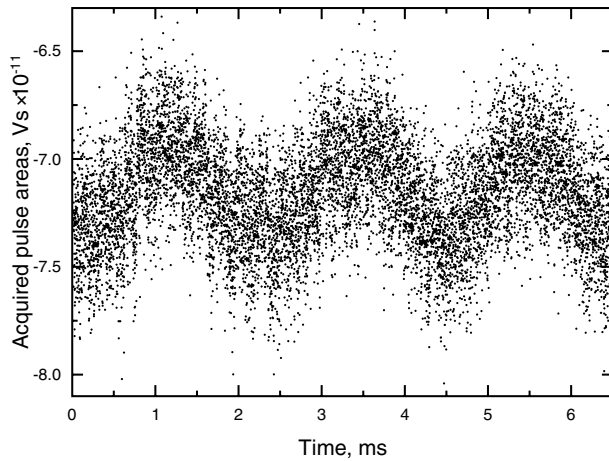


Figure 5 Acquired pulse areas as a function of the piezo scan. This signal is referred to a coherent state with a mean photon number of $\langle n \rangle = 0.16$ photons/pulse

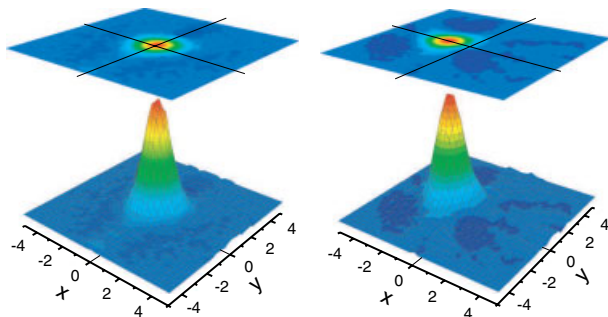


Figure 6 (online color at www.lphys.org) Reconstructed Wigner functions: (a) vacuum state; (b) weak coherent state with $\langle n \rangle \sim 1$ as obtained by IRT

distributions $p(x, \theta)$ for all values of θ allows the tomographic reconstruction of the quantum state of the radiation field as described in the previous section. In Fig. 6 we report the reconstructed Wigner functions in the case of the vacuum state (detected when the signal beam is blocked at the input of the homodyne beam splitter) and for a weak coherent field with a mean photon number $\langle n \rangle \sim 1$ as obtained by IRT.

We have also reconstructed the diagonal elements of the density matrix ρ_{nm} using Eq. (10) and the results are reported in Fig. 7 for three coherent states with different mean photon numbers. These values are well fitted by Poissonian distributions, as expected for coherent states.

5. Improved homodyne detector and gated acquisition

The time-domain analysis as discussed in the former sections has also been accomplished on a revised homodyne

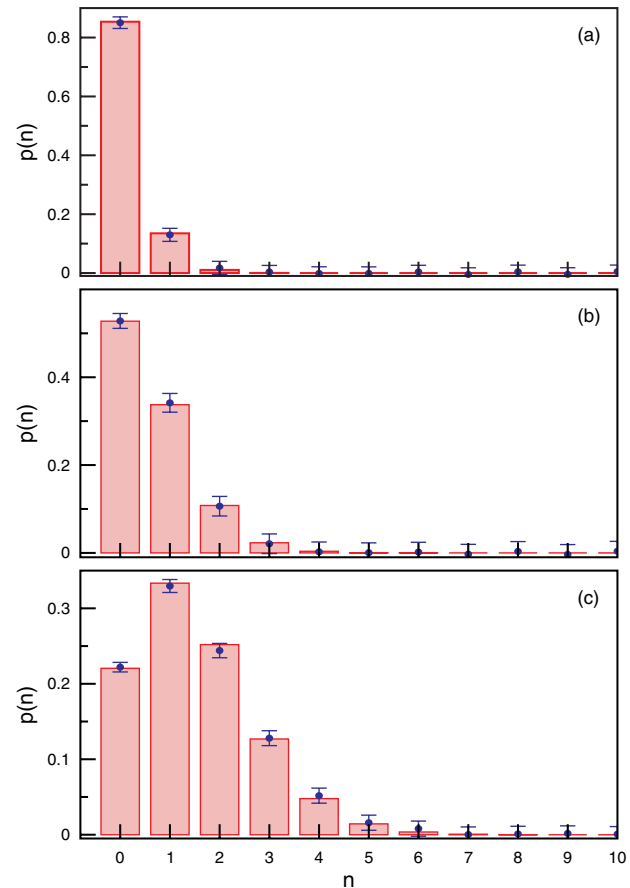


Figure 7 (online color at www.lphys.org) Reconstructed photon statistics of weak coherent states. The points with error bars are the reconstructed values. The boxes are best fit Poissonian distribution values with: (a) $\langle n \rangle = 0.16$ photons/pulse; (b) $\langle n \rangle = 0.64$ photons/pulse and (c) $\langle n \rangle = 1.5$ photons/pulse

detector scheme which reveals better performance with respect to linearity and signal-to-noise ratio. We have performed the acquisitions in a gated mode by selecting an ensemble of desired pulses to be analyzed by means of an external gate signal which triggers the acquisition.

Here the two PDs are connected to the positive and negative inputs of the operational amplifier with a feedback resistor which provides a gain of about 10. The amplifier output is now coupled in AC mode (to cut all the low-frequency noise) with a cut-off frequency of 1 MHz (at -3 dB). In this case, the signal is recorded by a different digital scope (Tektronix TDS7104) with an analog bandwidth of 1 GHz and a sampling rate of 10 Gsamples/s, a vertical resolution of 8 bits, and a memory depth of 16,000,000 points on a single channel. For the acquisition of the homodyne signal and also for the calibration, the scope is used in the Fast Frame Acquisition mode, where a single frame of 250 points is acquired when a trigger event occurs at the scope trigger channel. At 10 GS/s sampling rate, the scope is able to acquire a sequence of 5321 frames

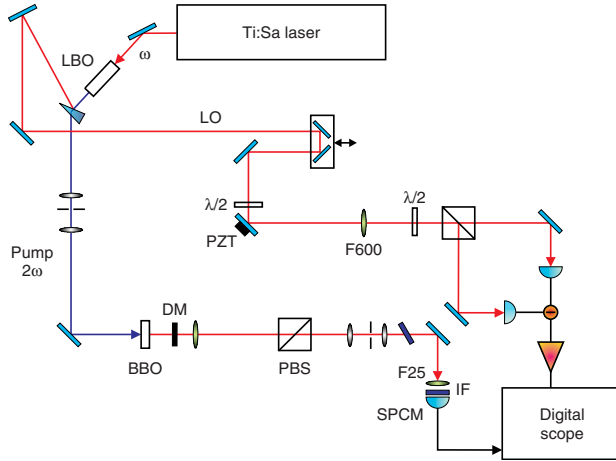


Figure 8 (online color at www.lphys.org) Calibration setup for the revised detector: the BBO crystal is used as a source for single photons that trigger the acquisition from the homodyne detector

of 250 points with a maximum rate of 160,000 frames per second. In this way each single acquired frame contains 2 laser pulses. The frames are then acquired in binary form via standard TCP/IP protocol network using the VISA software, achieving the maximum rate of one acquisition every 5 s. The downloaded frames are then elaborated by computer facilities allowing the measure of the area variances for the acquired pulses.

The acquisition of two nearby laser pulses allows the simultaneous analysis of the “signal” pulses, namely those pulses that have interfered with the signal beam, and of the dark pulses. Therefore, from each acquired scope frame we have contemporaneously the signal and shot-noise variance, free from low-frequency fluctuations that might be introduced by the electronics.

The trigger signal for the scope is generated from a single photon counting module (SPCM) which detects the filtered idler photons emitted by a BBO crystal of length 0.5 mm pumped by an UV pump as shown in the calibration setup of Fig. 8. As in the case of the former detector characterization, the local oscillator is provided by the laser pulses and it is split by a $\lambda/2$ wave-plate followed by a polarizing beam splitter (PBS). The second input port of the PBS is blocked in order to just measure the shot noise characteristics of the laser. The output ports of the PBS are detected by the two PDs of the homodyne detector.

Again, we have verified the ability of the detector to really measure the shot-noise by measuring the pulse difference area in a time-domain gated configuration as a function of the local oscillator power. Measurements have been carried out by inserting an amplifier with gain 10 and bandwidth dc-300 MHz (Phillips 770 NIM module) between the homodyne output and the digital scope. The scope vertical sensibility is set to 130 mV/div and the bandwidth is limited to 250 MHz. The CMRR is maximized by adjusting the $\lambda/2$ waveplate and the bias voltage

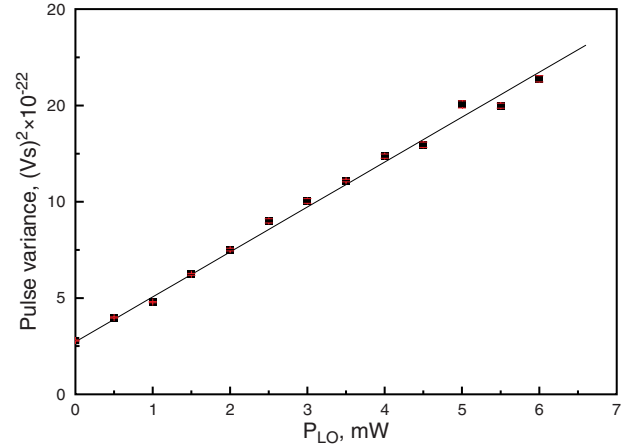


Figure 9 Measured pulse variance of the revised balanced homodyne detector as a function of the local oscillator power

of the two PDs, and it is found to be 34 dB at 81.5 MHz with the bias set to $V_{b+} = 50$ V and $V_{b-} = 35$ V.

The results show a linear behavior of the homodyne signal power noise over a wide range of LO powers, as reported in Fig. 9. The dark noise is at the same level of the previous detector, but the response is now linear for LO powers as high as 5-6 mW. The signal to noise ratio is improved to $S/N = 6$ dB when we operate at a local oscillator power of 5 mW.

6. Tomographic reconstruction of the single-photon Fock state

6.1. Generation of single-photon Fock states

A single-photon Fock state can be generated by means of a conditional state preparation on the two-photon wavefunction emitted in the process of spontaneous parametric down-conversion (SPDC) (see [36,37] and references therein). Such a state is written as

$$|\Psi\rangle = |0\rangle_s |0\rangle_t - \quad (18)$$

$$- \int d^3k_s d\omega_s d^3k_t d\omega_t \psi(\mathbf{k}_s, \omega_s, \mathbf{k}_t, \omega_t) |\mathbf{k}_s, \omega_s\rangle_s |\mathbf{k}_t, \omega_t\rangle_t,$$

where the function $\psi(\mathbf{k}_s, \omega_s, \mathbf{k}_t, \omega_t)$ describes the spatial and spectral properties of the two-photon state (*biphoton*) and the subscripts s and t correspond to the signal and trigger (idler) photons.

In order to non-locally select a pure state on the signal channel, trigger photons must undergo narrow spatial and frequency filtering before being detected by a single photon counter [36,38]. The conditional non-local preparation of the signal state is thus described by the density operator $\hat{\rho}_s$ given by the partial trace of the product between the

SPDC-state density operator and the measurement density operator $\hat{\rho}_t$:

$$\hat{\rho}_s = \text{Tr}[\hat{\rho}_t |\Psi\rangle\langle\Psi|]_t, \quad (19)$$

where

$$\hat{\rho}_t = \int d^3k_t d\omega_t T(\mathbf{k}_t, \omega_t) |\mathbf{k}_t, \omega_t\rangle_t \langle\mathbf{k}_t, \omega_t|_t \quad (20)$$

and $T(\mathbf{k}, \omega)$ is the transmission function of the spatial and spectral filter placed along the trigger photon path. Note that the nonlocally-prepared signal state will only approach a pure state if the filter transmission function $T(\mathbf{k}, \omega)$ is much narrower than the momentum and spectral widths of the pump beam generating the SPDC pair. Accordingly, one can define a purity parameter as $P = \text{Tr}(\hat{\rho}_s^2)$ which, in the spectral domain, is expressed as

$$P_t = \frac{1}{\sqrt{1 + \sigma_f^2/\sigma_p^2}}, \quad (21)$$

where Gaussian profiles with widths σ_p and σ_f are assumed for the pump power spectrum and for the trigger filter transmission, respectively. It is easy to see how the spectral purity parameter P_t approaches unity when $\sigma_f \ll \sigma_p$. In such a condition the strong spectral filtering performs a non-local selection of a pure signal state whose properties are defined by the pump as shown in [37,39]. Similarly, the spatial purity parameter is found to be [36]:

$$P_s = \frac{1}{1 + \kappa_i^2/\kappa_p^2}, \quad (22)$$

where κ_i and κ_p are the beam widths in the momentum space for the idler spatial filter and for the pump, respectively, and the missing square root with respect to Eq. (21) is connected with the two-dimensional nature of the spatial mode-matching.

6.2. Experimental setup

A mode-locked Ti:sapphire laser, emitting 1-2 ps long pulses at 786 nm with a repetition rate of 82 MHz is used as the primary source for the experiment, schematically drawn in Fig. 10. The laser pulses are first frequency doubled in a 13-mm long LBO crystal which produces the pump pulses centered at 393 nm, with a mean power of about 100 mW. The UV pump pulses, after a spatial mode cleaner, are then slightly focused, with a beam waist $w_p = 220 \mu\text{m}$, and the waist position is carefully located inside a 3-mm thick, Type I BBO crystal cut for collinear degenerate SPDC. The crystal is adjusted in order to obtain a signal-trigger cone beam with an angle of $\sim 3^\circ$. Signal and trigger photon pairs are then selected by means of irises placed at 70 cm from the output face of the crystal.

The trigger beam is directed to the state preparation channel, where it is spectrally filtered by means of a pair of

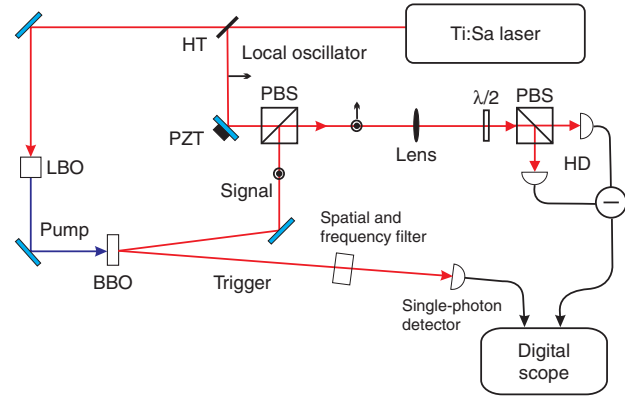


Figure 10 (online color at www.lphys.org) Experimental apparatus: HT high-transmission beamsplitter, LBO second harmonic generation crystal, BBO downconverter crystal, PZT piezoelectric transducer, PBS polarizing beamsplitter, $\lambda/2$ half-wave plate, HD homodyne detector

etalon interference filters and is then coupled into a single-mode fiber connected to a single photon counting module with an active-area diameter of $200 \mu\text{m}$ (Perkin-Elmer SPCM AQR-14). The typical trigger count rate after spectral and spatial filtering is of about 500 s^{-1} .

The combination of the two etalon cavities yields a final spectral width for the trigger channel of about 50 GHz. By comparing this with a measured pump width of 430 GHz, we estimate a spectral purity parameter of $P_t = 0.98$. However, due to the second harmonic generation process, the LO spectral width remains $\sqrt{2}$ times narrower than that of the selected single-photon state. The degree of mode-matching between the LO and the single-photon state cannot be improved by filtering the LO beam and might be increased only by inserting a spectral filter on the UV pump. However, this solution would also drastically lower the count rate on the trigger detector and has not been implemented yet.

Filtering in the spatial domain is achieved by means of the single-mode fiber and our experimental parameters lead to a spatial purity parameter $P_s = 0.86$, which again means that the conditionally prepared single-photon state mode is essentially determined by the pump characteristics. The LO beam is spatially mode-matched to the fiber-selected signal mode by the insertion of appropriate lens combinations along its path. In order to finely adjust the alignment and the synchronization between the signal and LO pulses, we use the stimulated beam produced by injecting a seed pulse into the crystal. Under appropriate conditions [36], the amplified seeded beam can spatially well simulate the selected signal beam and can be used for alignment purposes.

The LO pulses are obtained by splitting a small portion of the laser emission, and their polarization is rotated by a half-wave plate in order to overlap them with the conditionally-prepared single-photon signal beam onto a

polarizing beam splitter (PBS). One of the steering mirrors is mounted on a piezoelectric transducer in order to vary and control the LO phase. A 300-mm focal-length lens, an additional $\lambda/2$ wave plate, and a second PBS are then used to accurately mix the two field modes and focus them onto the two photodiodes of the homodyne detector.

6.3. High-frequency balanced homodyne detection

Two different photodiodes (Hamamatsu S3883, with active area 1.7 mm^2) are connected to the positive and negative inputs of the operational amplifier as described in Sec. 5. The performances of the detector used for this experiment show a linear response up to LO powers of 9 mW, and with a signal-to-noise ratio of about 12 dB when the device is operated at the optimum LO power of 7 mW which is used for all the homodyne measurements for the Fock state.

In order to decrease the effect of the dark counts in the single-photon trigger detector, a strict coincidence with the signal coming from the laser pulse train is used as the trigger for the acquisition of the homodyne signal. Although this slightly reduces the trigger count rate, it is effective in increasing the ratio of “true” to “false” trigger events to more than 99%. The average rate of trigger counts is thus about 300 s^{-1} and each sequence is acquired in about 15–20 s, yielding an experimental Wigner marginal distribution in just about 30 s.

It is interesting to compare these acquisition times with those reported in [16] by the Constance group for the first tomographic reconstruction of the single-photon Fock state. Due to the limited bandwidth of their homodyne detector (1 MHz), the overall pulse rate had to be lowered to about 800 kHz by means of a pulse picker at the exit of the laser. In that case about 12,000 experimental data points were acquired in a 14-hour experimental run in order to obtain an accurate phase-averaged marginal distribution of the quantum state. Our setup now allows the same kind of acquisition to be performed in just about one minute, with a gain of almost three orders of magnitude in the measurement time. It is clear that such a speed-up can help to loosen some of the constraints on the overall stability of the generation system and, in particular, on the interferometric stability of the beam paths which is needed when phase-dependent quantum states are to be analyzed. On the other hand, by greatly increasing the overall number of available LO pulses in a reasonable experimental time interval, our scheme will allow us to investigate much rarer and more exotic events, such as those involving higher photon numbers [26, 40].

Note that recent experiments from the same group [20, 41] have seen the adoption of a clever solution to the limited acquisition rate caused by the low detector bandwidth. Instead of reducing the whole experimental repetition rate, the pulse picker has been placed only in the LO path and

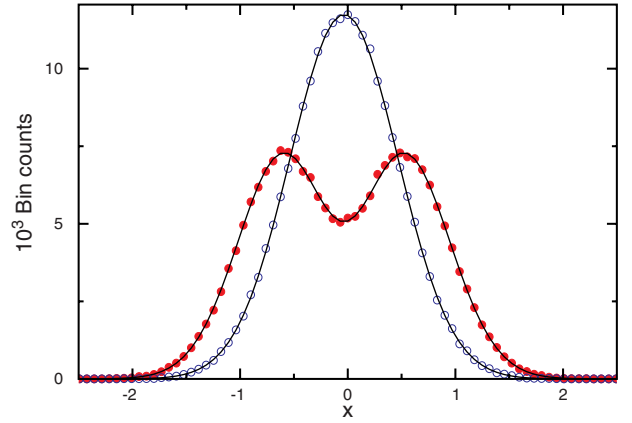


Figure 11 (online color at www.lphys.org) Vacuum (open circles) and signal (filled circles) phase-averaged quadrature field distributions. The solid lines are fitted curves. The x -axis is normalized to the $1/e^2$ half width of the shot noise (vacuum) distribution

activated “on demand” upon a trigger detection event. This has allowed to keep reasonable pair production rates and to obtain a final acquisition rate similar to the one presented here. However, the introduction of the pulse picker, besides significantly complicating the experimental setup, has the important drawback that the trigger delay of the shutter in the LO path has to be compensated by a long (about 15 m) optical delay line on the signal photon path in order for the two to reach the mixing beam-splitter at the same time. This clearly introduces additional losses and may degrade both the mode quality and the accurate phase stability of the fragile quantum state.

6.4. Quantum state reconstruction

The distributions of the acquired pulse areas for the vacuum and the single-photon state are shown in Fig. 11, where each histogram is obtained from the analysis of about 200,000 acquired pulses.

The non-unity detection efficiency of the apparatus prevents us from observing the real single-photon Wigner function, and what we get instead is its convolution with the vacuum one. The convolution result is the well known s -parametrized quasi-probability distribution with the s parameter scaled by the detection efficiency η [6, 42]. The expression for the corresponding marginal distribution is:

$$p(x; \eta) = \sqrt{\frac{2}{\pi}} [1 - \eta(1 - 4x^2)] e^{-2x^2}. \quad (23)$$

From a fit of the experimental distributions to the corresponding theoretical curves we obtain an overall detection efficiency of $\eta = 0.574 \pm 0.002$.

The expected overall efficiency η is given by the contribution of several terms:

$$\eta = \eta_{\text{hd}} \eta_{\text{dc}} \eta_{\text{mm}} \quad (24)$$

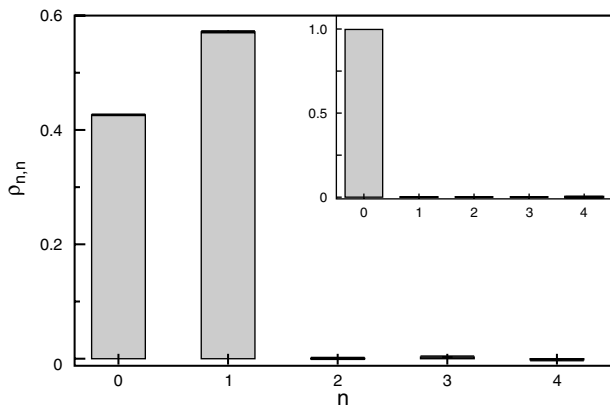


Figure 12 Reconstructed diagonal elements of the density matrix for the single-photon state and the vacuum (inset)

where $\eta_{hd} = 0.90$ is the efficiency of the homodyne detector including the PBS losses, while $\eta_{dc} = 0.99$ is the efficiency connected to the dark counts of the trigger detector. The mode-matching efficiency is given by $\eta_{mm} = \eta_{exp} \sqrt{P_s P_t}$, where $\sqrt{P_s P_t}$ depends on the tightness of the spatial and spectral filtering on the trigger channel and constitutes the upper limit for the mode-matching efficiency achievable between a pure state (LO) and the non-locally selected single photon state. The term η_{exp} is connected with the non-ideal experimental conditions and can be estimated from the visibility of the interference fringes formed between the LO and the stimulated radiation used for alignment [36]. We obtain $\eta_{exp} \simeq 0.7$ and the overall efficiency is thus expected to be $\eta \simeq 0.6$, in good agreement with the value retrieved from the fit of the marginal data to the theoretical distributions.

In Fig. 12 the reconstructed diagonal elements $\rho_{n,n}$ of the density matrix are reported as obtained with Eq. 10. This figure clearly shows the non-poissonian photon distribution of the reconstructed state, which is a statistical mixture of the single-photon Fock state with the vacuum state $\hat{\rho} = \rho_{0,0}|0\rangle\langle 0| + \rho_{1,1}|1\rangle\langle 1|$ with $\rho_{0,0} = 0.426 \pm 0.001$ and $\rho_{1,1} = 0.572 \pm 0.002$ in good agreement with the efficiency value found by fitting the marginal distributions.

In Fig. 13 we show the Wigner function obtained from the first 10 reconstructed diagonal elements of the density matrix and by setting all the off-diagonal terms to zero thanks to the phase-invariance of the state. The reconstructed Wigner function assumes negative values at the origin, showing the non-classical features of the single-photon state. We find $W_{meas}(0,0) = -0.0995$, which is quite close to the theoretical value of the Wigner function $W(0,0;\eta) = -0.0942$ obtained by using Eq. (14) with the mixed state defined by

$$\hat{\rho} = (1 - \eta)|0\rangle\langle 0| + \eta|1\rangle\langle 1| \quad (25)$$

with the efficiency value ($\eta = 0.574$) retrieved from the fit of the phase-averaged marginal distributions.

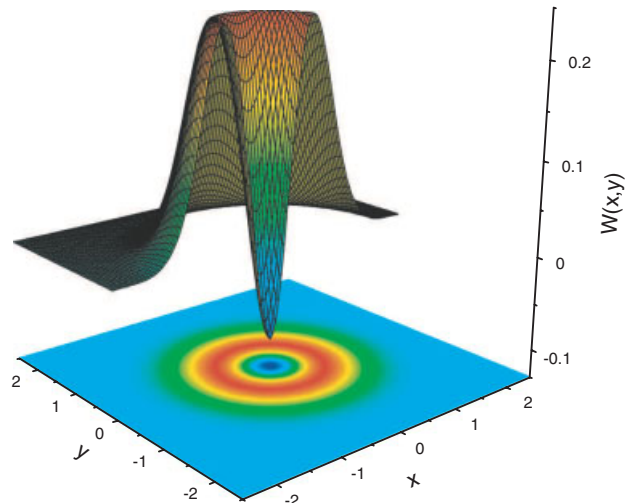


Figure 13 (online color at www.lphys.org) Wigner function of the single-photon Fock state as obtained from the reconstructed density-matrix elements. The negativity of the distribution, a clear proof of the non-classical character of the state, is evident around the origin of the shot-noise normalized quadrature axes

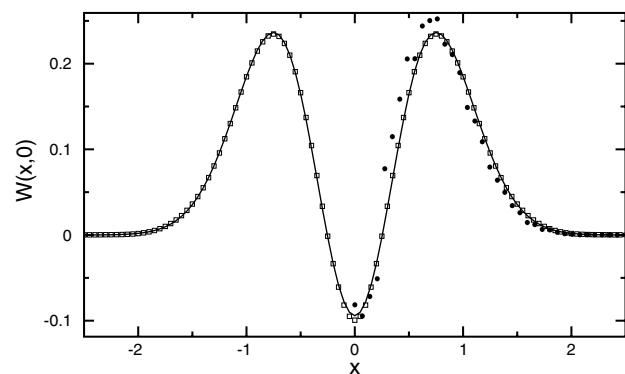


Figure 14 $W(x,0)$ section of the reconstructed Wigner function as a function of the normalized quadrature x . Filled circles: Abel transform; empty squares: section of Fig.13; solid line: section corresponding to the mixed state of Eq. (25)

A comparison between the different methods of Wigner function reconstruction is presented in Fig. 14 where the $W(x,0)$ section is plotted. Both the profile obtained by a direct implementation of the Abel transform on the acquired homodyne histograms using the basic algorithm of Nestor and Olsen [43] and a section of the Wigner function as reported in Fig. 13 are shown, together with the curve retrieved using the mixed state of Eq. (25). The direct reconstruction method based on the Abel transform is extremely sensitive to the noise present in the data and fails to accurately reproduce the expected vacuum-convoluted single-photon Wigner function. The accuracy of this kind of reconstruction might only be improved by using a larger set of experimental data with smaller statistical noise. On

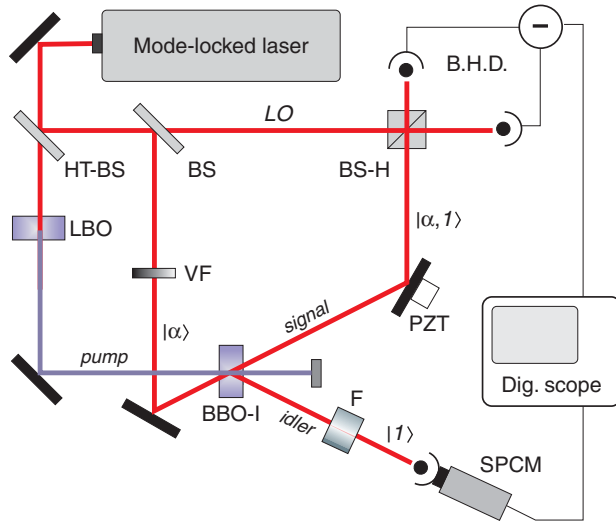


Figure 15 (online color at www.lphys.org) Experimental apparatus: HT-BS high transmission beam-splitter, LBO lithium triborate crystal, BS and BS-H 50% beam-splitters, VF variable attenuation filter, BBO-I type-I β -barium borate down-converter crystal, PZT piezoelectric transducer, B.H.D. balanced homodyne detector, F spectral and spatial filters, SPCM single photon counting module

the other hand, when the same data set is used for the reconstruction via the density-matrix elements, the resulting curve is much closer to the expected profile thanks to the limited number ($M=10$) of elements used to describe the quantum state.

7. Single-photon-added coherent states

The high-frequency homodyne detector has also been recently used to analyze a new class of quantum field states. Single-photon-added coherent states result from the elementary excitation by a single quantum of a coherent state and possess intermediate properties between those of Fock and coherent states. While a coherent state $|\alpha\rangle$ is the closest analogue to a classical light field and possesses well defined amplitude and phase, with minimal fluctuations permitted by the uncertainty principle, a Fock state $|n\rangle$ is on the contrary strictly quantum-mechanical and contains a precisely defined number of quanta of field excitation, hence its phase is completely undefined. Single-photon-added coherent states are particularly interesting from a fundamental point of view since their degree of non-classicality can be continuously tuned between the two extreme situations of pure quantum and classical states described above [28].

Single-photon-added coherent states (SPACSs) are generated by the action of the photon creation operator on a coherent state [44] and read as:

$$|\alpha, 1\rangle = \frac{\hat{a}^\dagger |\alpha\rangle}{\sqrt{1 + |\alpha|^2}}. \quad (26)$$

Unlike the operation of photon annihilation, which maps a coherent state into a coherent state (i.e. a classical field into another classical field), a single-photon excitation of a coherent state changes a classical state into a quantum state with a varying degree of non-classicality which becomes more evident the smaller the initial amplitude of the $|\alpha\rangle$ state. In the extreme case of an initial vacuum state $|0\rangle$, a single excitation event transforms it into the very non-classical single-photon Fock state $|1\rangle$, which exhibits negative values of the Wigner function around the origin [16, 27]. The negativity of the Wigner function [6, 41, 42], is indeed a good indication of the highly non-classical character of the state.

7.1. Generation of SPACS

In order to generate SPACS one has to inject a seed coherent field $|\alpha\rangle$ into the signal mode of the parametric amplifier and the conditional preparation of the target state takes place every time that a single photon is detected in the correlated idler mode. If the parametric gain is kept sufficiently low, which is always the case in our experimental situation, the final output state can be approximated as

$$|\Psi\rangle = (1 + g\hat{a}_s^\dagger\hat{a}_i^\dagger)|\alpha\rangle_s|0\rangle_i = |\alpha\rangle_s|0\rangle_i + g\hat{a}_s^\dagger|\alpha\rangle_s|1\rangle_i, \quad (27)$$

(here g is a gain constant with $|g| \ll 1$) and the output signal mode will contain the original coherent state most of the times, except for the few cases when the state is detected in the idler output mode; these relatively rare detection events project the signal state into the SPACS $|\alpha, 1\rangle_s$, which corresponds to the stimulated emission of one photon in the same mode of $|\alpha\rangle$. Note that the absence of a seed coherent field leaves with the usual expression for the spontaneous process so that, by studying the evolution of the quantum state while the amplitude α gradually increases from zero, one can actually witness the smooth transition from the spontaneous to the stimulated regimes of light emission with the transformation of an initial purely-quantum state (the single-photon Fock state) into a classical coherent one. This is accompanied by the birth of a well-defined phase and can be described in more visual terms as the transition from the particle-like to the wave-like behaviors of the electromagnetic field.

The experimental apparatus used to generate and analyze the SPACS is very similar to that used in Sec. 6 and is schematically drawn in Fig. 15. The weak coherent state $|\alpha\rangle$ is obtained by controlled attenuation of a small portion of the laser emission which is fed to the nonlinear crystal into the signal mode.

7.2. Quantum homodyne detection and reconstruction

The detection apparatus as described in Sec. 6.3 is used for the homodyne detection of SPACSs at different seed

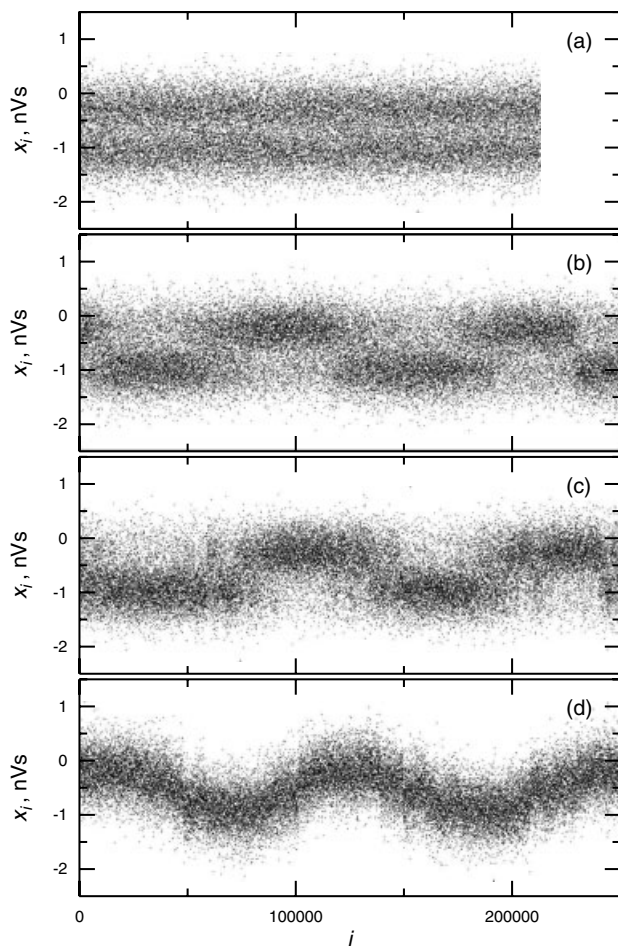


Figure 16 Homodyne data for SPACS with a) $|\alpha| = 0$, i.e. the single photon Fock state is generated; b) $|\alpha| = 0.387$; c) $|\alpha| = 0.723$; d) $|\alpha| = 3.74$

coherent state amplitudes. In Fig. 16 the acquired homodyne data are reported as a function of the PZT position. The first plot (Fig. 16a), obtained with a blocked input, corresponds to the single-photon Fock state (cfr. Sec. 6). When the coherent seed is initially switched on at very low intensity, data show the appearance of higher density regions due to the gradual appearance of a defined phase (Fig. 16b). Finally, for increasing seed amplitudes (Fig. 16c and Fig. 16d), the signal distributions become more and more similar to those of a classical coherent field (cfr. Fig. 5). Fig. 17 finally presents the reconstructed Wigner function corresponding to a SPACS with $|\alpha| = 0.387$ which clearly shows negative values as a proof of the nonclassical character of the state.

It should be noted that the overall detection efficiency of the system is now about 60% and that, contrary to the situation of Sec. 4, the coherent state amplitude α does not include the effects of limited efficiency [45]. The reconstructed Wigner function is obtained first calculating the density matrix elements with Eq. (11) using the ho-

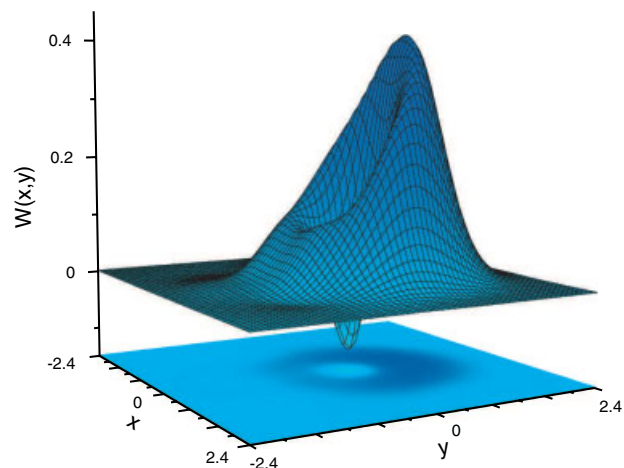


Figure 17 (online color at www.lphys.org) Reconstructed Wigner function for SPACS with $|\alpha| = 0.387$

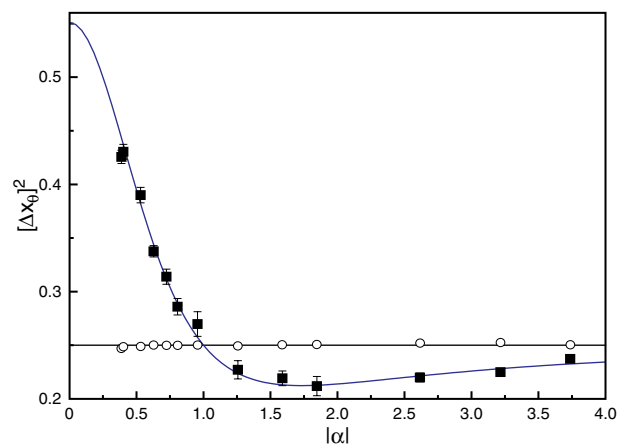


Figure 18 (online color at www.lphys.org) Variances of the squeezed (filled squares) quadrature of the SPACS for different coherent state amplitudes. Also shown are the experimental data (empty circles) and the theoretical curve (horizontal line at 1/4) for the variance of the coherent state

modyne data of Fig. 16b then the transformation (14) is applied with $M = 6$.

The nonclassical nature of the SPACSs is also evident from a measurement of the variance of a field quadrature for different values of the amplitude α . Fig. 18 clearly shows a pronounced squeezing of the corresponding fluctuations with respect to the coherent state ones measured in the same run.

8. Conclusions

In this brief review we have described an homodyne detection apparatus that is able to work at high-frequency in the

time-domain and gives access to the analysis of quantum light states generated by pulsed radiation at high repetition rates. We have investigated the main features of a time-resolved analysis of the homodyne signal, characterizing the system response and comparing it to a more standard spectral analysis. We have also shown that our apparatus allows pulse-selective measurements at very high repetition rates, a peculiarity which is particularly useful for the study of rare, conditionally-selected, events.

With respect to other current setups, operating well below the megahertz, our approach allows an improvement of at least two orders of magnitude in the acquisition rate. This results in two fundamental advantages: on one side, the stability requirements of the overall experimental system are loosened; on the other, if long-term stability of the setup is available, it is possible to reconstruct states with higher photon numbers, characterized by a smaller generation probability.

Finally, we have illustrated a few examples of the application of this time-domain homodyne detector to perform quantum tomographic reconstructions of special classical and quantum states, including coherent, Fock and single-photon-added coherent states. The very good characteristics of flexibility and efficiency of the apparatus will make it a precious tool to explore the quantum world with the analysis of novel field states.

Acknowledgements This work has been performed in the frame of the "Spettroscopia laser e ottica quantistica" project of the Department of Physics of the University of Florence and partially supported by the Italian Ministry of University and Scientific Research (MIUR), under the FIRB contract RBNE01KZ94.

References

- [1] H.P. Yuen and J.H. Shapiro, in: L. Mandel and E. Wolf (eds.), *Coherence and Quantum Optics IV* (Plenum, New York, 1978).
- [2] H.P. Yuen and V.W.S. Chan, *Opt. Lett.* **8**, 177 (1983).
- [3] G.L. Abbas, V.W.S. Chan, and T.K. Yee, *Opt. Lett.* **8**, 419 (1983).
- [4] K. Vogel and H. Risken, *Phys. Rev. A* **40**, 2847 (1989).
- [5] S. Reynaud, A. Heidmann, E. Giacobino, and C. Fabre, in: E. Wolf (ed.), *Progress in Optics* **30** (Elsevier, Amsterdam, 1992), p. 1.
- [6] U. Leonhardt, *Measuring the quantum state of light* (Cambridge University Press, Cambridge, England, 1997).
- [7] G.M. D'Ariano, in: T. Hakiolu and A.S. Shumovsky (eds.), *Quantum Optics and Spectroscopy of Solids* (Kluwer Academic Publishers, 1997), p. 175.
- [8] D.T. Smithey, M. Beck, M.G. Raymer, and A. Faridani, *Phys. Rev. Lett.* **70**, 1244 (1993).
- [9] D.T. Smithey, M. Beck, J. Cooper, and M.G. Raymer, *Phys. Rev. A* **48**, 3159 (1993).
- [10] G. Breitenbach, S. Schiller, and J. Mlynek, *Nature* **387**, 471 (1997).
- [11] G. Breitenbach and S. Schiller, *J. Mod. Opt.* **44**, 2207 (1997).
- [12] A. Zavatta, F. Marin, and G. Giacomelli, *Phys. Rev. A* **66**, 043805 (2002).
- [13] V. D'Auria, A. Chiummo, M.D. Lurentis, et al., *Opt. Express* **13**, 948 (2005).
- [14] M. Vasilyev, S.-K. Choi, P. Kumar, and G.M. D'Ariano, *Opt. Lett.* **23**, 1393 (1998).
- [15] M. Vasilyev, S.-K. Choi, P. Kumar, and G.M. D'Ariano, *Phys. Rev. Lett.* **84**, 2354 (2000).
- [16] A.I. Lvovsky, H. Hansen, T. Aichele, et al., *Phys. Rev. Lett.* **87**, 050402 (2001).
- [17] A.I. Lvovsky and S.A. Babichev, *Phys. Rev. A* **66**, 011801 (2002).
- [18] A.I. Lvovsky and J. Mlynek, *Phys. Rev. Lett.* **88**, 250401 (2002).
- [19] S.A. Babichev, J. Ries, and A.I. Lvovsky, *Europhysics Lett.* **64**, 1 (2003).
- [20] S.A. Babichev, B. Brezger, and A.I. Lvovsky, *Phys. Rev. Lett.* **92**, 047903 (2004).
- [21] S.A. Babichev, J. Appel, and A.I. Lvovsky, *Phys. Rev. Lett.* **92**, 193601 (2004).
- [22] J. Wenger, R. Tualle-Brouiri, and P. Grangier, *Phys. Rev. Lett.* **92**, 153601 (2004).
- [23] M. Crispino, G.D. Giuseppe, F. De Martini, and P. Mataloni, *Fortschr. Phys.* **48**, 589 (2000).
- [24] H. Hansen, T. Aichele, C. Hettich, et al., *Opt. Lett.* **26**, 1714 (2001).
- [25] J. Wenger, R. Tualle-Brouiri, and P. Grangier, *Opt. Lett.* **29**, 1267 (2004).
- [26] A. Zavatta, M. Bellini, P.L. Ramazza, et al., *J. Opt. Soc. Am. B* **19**, 1189 (2002).
- [27] A. Zavatta, S. Viciani, and M. Bellini, *Phys. Rev. A* **70**, 053821 (2004).
- [28] A. Zavatta, S. Viciani, and M. Bellini, *Science* **306**, 660 (2004).
- [29] B.L. Schumaker, *Opt. Lett.* **9**, 189 (1984).
- [30] B. Yurke and D. Stoler, *Phys. Rev. A* **36**, 1955 (1987).
- [31] G.M. D'Ariano, C. Macchiavello, and M.G.A. Paris, *Phys. Rev. A* **50**, 4298 (1994).
- [32] G.M. D'Ariano, *Quantum Semiclass. Opt.* **7**, 693 (1995).
- [33] K. Banaszek, G.M. D'Ariano, M.G.A. Paris, and M.F. Sacchi, *Phys. Rev. A* **61**, 010304 (1999).
- [34] A.I. Lvovsky, *J. Opt. B: Quantum Semiclassical Opt.* **6**, S556 (2003).
- [35] D.W. Allan, *Proc. IEEE* **54**, 221 (1966).
- [36] T. Aichele, A.I. Lvovsky, and S. Schiller, *Eur. Phys. J. D* **18**, 237 (2002).
- [37] S. Viciani, A. Zavatta, and M. Bellini, *Phys. Rev. A* **69**, 053801 (2004).
- [38] Z.Y. Ou, *Quantum Semiclass. Opt.* **9**, 599 (1997).
- [39] M. Bellini, F. Marin, S. Viciani, et al., *Phys. Rev. Lett.* **90**, 043602 (2003).
- [40] A. Montina and F.T. Arecchi, *Phys. Rev. A* **58**, 3472 (1998).
- [41] A.I. Lvovsky and J.H. Shapiro, *Phys. Rev. A* **65**, 033830 (2002).
- [42] L. Mandel and E. Wolf, *Optical Coherence and Quantum Optics* (Cambridge University Press, Cambridge, 1995).
- [43] C.J. Cremers and C. Birkebak, *Appl. Opt.* **5**, 1057 (1966).
- [44] G.S. Agarwal and K. Tara, *Phys. Rev. A* **43**, 492 (1991).
- [45] A. Zavatta, S. Viciani, and M. Bellini, *Phys. Rev. A* **72**, 023820 (2005).